

## The Infrared Cloud Monitor for the MAGNUM Robotic Telescope at Haleakala

MASAHIRO SUGANUMA,<sup>1</sup> YUKIYASU KOBAYASHI,<sup>1</sup> NORIO OKADA,<sup>1</sup> YUZURU YOSHII,<sup>2,3</sup> TAKEO MINEZAKI,<sup>2</sup> TSUTOMU AOKI,<sup>4</sup>  
KEIGO ENYA,<sup>5</sup> HIROYUKI TOMITA,<sup>4</sup> AND SHINTARO KOSHIDA<sup>1,6</sup>  
*Received 2006 April 1; accepted 2007 April 5; published 2007 May 24*

**ABSTRACT.** We present the most successful infrared cloud monitor for a robotic telescope. The system was originally developed for the MAGNUM 2 m telescope, which has been achieving unmanned, automated monitoring observations of active galactic nuclei at Haleakala on the Hawaiian island of Maui since 2001. Using a thermal imager and two aspherical mirrors, it sees at once almost the whole sky at a wavelength of  $\lambda \sim 10 \mu\text{m}$ . Its outdoor component is weatherproof and is totally maintenance-free. The images obtained every 1 or 2 minutes are categorized immediately into several ranks of weather conditions, from which our automated observing system not only decides whether to open or close the dome, but also selects what types of observations should be made. The whole-sky data accumulated over 4 years show that 50%–60% of all nights are photometric, and about 75% are observable with respect to cloud conditions at Haleakala. Many copies of this system are now used all over the world, such as those in Mauna Kea in Hawaii, Atacama in Chile, and Okayama and Kiso in Japan.

*Online material:* color figure

### 1. INTRODUCTION

A cloud-monitoring system that watches the sky to detect clouds above an observatory is a powerful apparatus for ground-based telescopes if we want to check the sky easily and execute remote or automated observations. Telescopes and their instruments are sure to be safe if we can accurately monitor clouds and close the dome slits before cloud cover becomes heavy and rain develops. Other types of weather monitors, such as rain or humidity sensors, sometimes alert us too late close the dome. With a cloud monitor, we can also determine whether or not the data acquired by the telescope have been affected by clouds.

One of the smartest methods of observing clouds from the ground is to use the thermal infrared wave bands in which clouds themselves emit thermal radiation or reflect radiation originating from the ground or sea. A CCD camera with a fish-eye lens is cheap, but the appearance of clouds in the optical is deceptive, because their brightness depends strongly on the intensity of the Moon and city lights that illuminate them. Using

a similar system, Shamir & Nemiroff (2005) developed an algorithm to make a whole-sky opacity map by means of measuring the extinction for many stars. However, it does not give us a direct view of the cloud distribution in the sky.

An uncooled thermal imager with panoramic optics suits a robotic telescope because it requires little maintenance. The Sloan Digital Sky Survey (SDSS) project has developed a scanning system using a single-channel photometer cooled by liquid nitrogen (Hull et al. 1994; Hogg et al. 2001). Its sensitivity and field of view is sufficient, but the scanning mechanism is not easy to construct, and its cooling system needs frequent maintenance. Recently, thermal infrared imagers without cooling parts yet sensitive enough to detect thin clouds have become available, and by combining these with some panoramic optics, we can now easily see the whole sky in thermal infrared. This idea was presented by Mallama & Degnan (2002), and a similar method was developed by the Apache Point Observatory.<sup>7</sup> However, stability and reliability are required in order for these systems to be put into practical use for a robotic telescope where no operator or engineer is on site.

We have developed an infrared cloud-monitoring system that is successful for this use. With this system, we have achieved unmanned automated observation at the MAGNUM observatory at Haleakala since 2001 (Kobayashi et al. 2003, 2004). The MAGNUM (Multicolor Active Galactic Nuclei Monitoring) project built a new 2 m optical-infrared telescope on the site of the University of Hawaii's Haleakala Observatory on the Hawaiian island of Maui, and has been monitoring many active galaxies and quasars in optical and near-infrared wave

---

<sup>1</sup> National Astronomical Observatory, Mitaka, Tokyo, Japan; suganuma@merope.mtk.nao.ac.jp.

<sup>2</sup> Institute of Astronomy, School of Science, University of Tokyo, Mitaka, Tokyo, Japan.

<sup>3</sup> Research Center for the Early universe, School of Science, University of Tokyo, Bunkyo-ku, Tokyo, Japan.

<sup>4</sup> Kiso Observatory, Institute of Astronomy, School of Science, University of Tokyo, Kiso, Nagano, Japan.

<sup>5</sup> Institute of Space and Astronomical Science, Japan Aerospace Exploration Agency, Sagami-hara, Kanagawa, Japan.

<sup>6</sup> Department of Astronomy, School of Science, University of Tokyo, Bunkyo-ku, Tokyo, Japan.

---

<sup>7</sup> See <http://irsc.apo.nmsu.edu>.

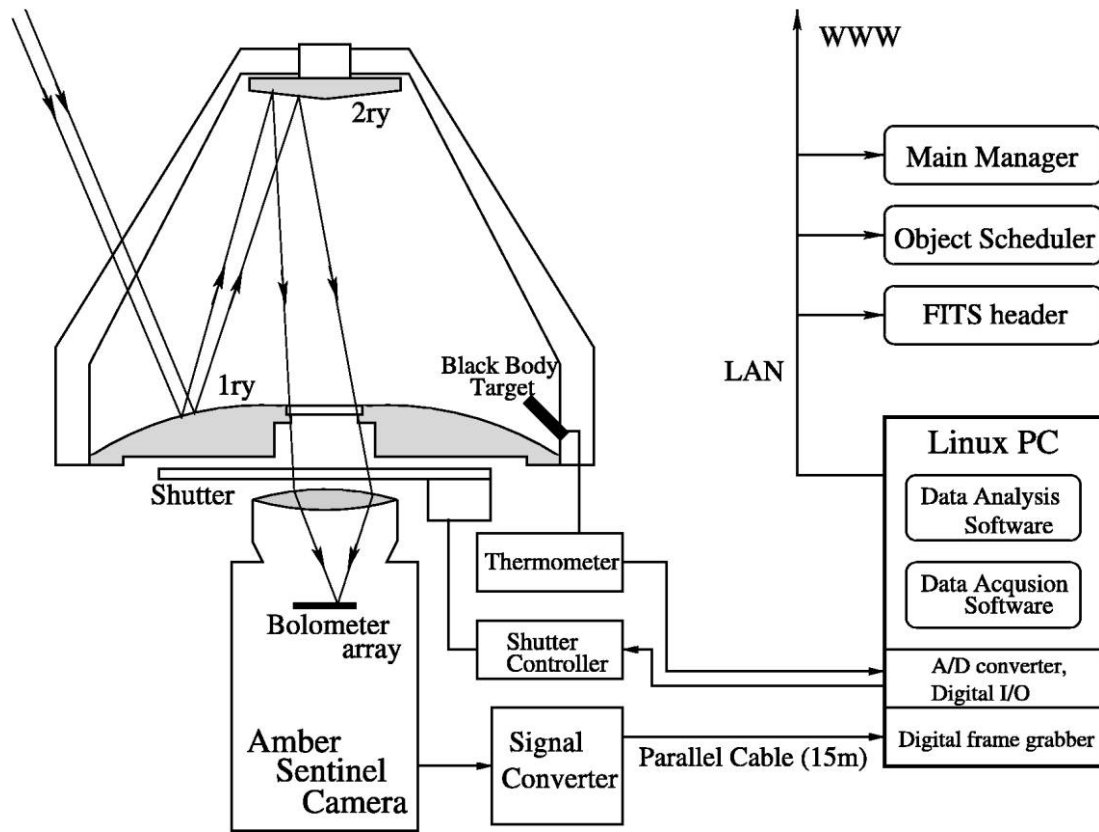


FIG. 1.—Schematic diagram of the MAGNUM infrared cloud monitor system. The outdoor hardware is on the left side of the figure, and the indoor hardware is at bottom right.

bands for more than a few years (Yoshii et al. 2003). We study their structure and physical environment, and finally determine the cosmological parameters using an entirely original method (Kobayashi et al. 1998; Yoshii 2002). The other distinct challenge of this project is to achieve unmanned automated observation. We aimed at and have achieved months-long automated observation without requiring anyone to be at the observatory.

In order to achieve this purpose, our whole-sky infrared cloud monitor has many salient characteristics for automated operation. It can see almost the whole sky at once in a thermal infrared wave band with a sensitivity that is high enough to detect thin clouds. It is weatherproof and has been outdoors under harsh weather conditions on top of a high-altitude mountain (about 3000 m high) for many years. Furthermore, the raw whole-sky images are immediately reduced to apparent emissivity maps of the cloud, which are then classified into several types of observational conditions. These maps and rankings can be referred to by our automated observing system and by the remote observers in Japan. They are also referred to by many facilities other than the MAGNUM telescope at Haleakala. Following our success, systems using copies of our design have been used at several observatories and sites, such as those

at Mauna Kea in Hawaii (Takato et al. 2002), Atacama in Chile, and Okayama and Kiso in Japan. These systems encourage studies of sites for new observatories where it is difficult for people to remain for any length of time.

In this paper, we describe our infrared cloud monitor system, breaking it down into its design, hardware contents, data analysis software, and performance and statistical data. The main instrument design and its components, including the thermal imager, reflecting optics, and data acquisition system, are described in § 2. Section 3 describes the analysis software that detects clouds and evaluates the whole-sky condition. The operational performance of the MAGNUM observatory is presented and discussed in § 4. Finally, weather trends seen in our whole-sky-condition data, accumulated over 4 years, are discussed in § 5.

## 2. SYSTEM OVERVIEW

Figure 1 shows a schematic diagram of the MAGNUM Infrared Cloud Monitor. The outdoor hardware of the system is on the left side of the figure. There are two aspherical convex mirrors with Cassegrain-like alignment. A blackbody reference plate for calibration is installed where the camera can see it

near the edge of its field of view. All electrical devices, including the thermal imager, signal converter for the output signal of the imager, shutter, and thermometer circuit for the blackbody reference plate, are attached under the primary mirror and surrounded by an aluminum pipe housing whose ceiling is the primary mirror. On the central hole of the primary mirror is installed a diamond window that is transparent to thermal infrared and prevents water from dripping into the housing. Photographs of the outdoor hardware are shown in Figures 2 and 3. The unit is about 80 cm in height and about 35 cm in diameter.

The data collected by the outdoor hardware are acquired by a Linux PC, illustrated on the lower right side of Figure 1. The PC controls the shutter with a digital I/O board and also triggers data acquisition of images and temperatures. The controlling and data acquisition software, as well as the analysis software, are always running, collecting sets of data, including whole-sky raw images every 1 or 2 minutes throughout the night. The output data are directed to various types of software through a LAN in the MAGNUM observatory that includes the main manager of the observatory, the real-time scheduler or selector of target astronomical objects, and the information-collecting server for image headers of astronomical observations.<sup>8</sup>

The specifications of our infrared cloud monitor are listed in Table 1. Owing to the uncooled thermal imager and reflecting optics that widen the camera field of view, we can obtain almost whole-sky images in thermal infrared. This hardware alignment, a Cassegrain-like mirror system above an aluminum pipe housing containing the thermal imager and electronic parts, has a significant advantage in that the outdoor system is compact and waterproof. The only movable component in the system is a shutter, a Prontor magnetic E/100 shutter, which works both as a shield against the sunlight during daytime and as a flat-fielding plate for image reduction.

The main hardware components of our infrared cloud monitor are the thermal imager, the reflecting optics, and the data acquisition system, the details of which are described individually below.

### 2.1. Thermal Imager

The uncooled infrared imager, which is sensitive in the 10  $\mu\text{m}$  wave band, is one of the key components of our cloud monitor. In order to see high-altitude clouds with good visibility or to detect the thermal emission of clouds standing out against the dark background of cold space, we need to select a wave band in which the atmosphere is highly transparent. There are two wave bands satisfying this requirement: one is the 3 ~ 5  $\mu\text{m}$  band, and the other is the 10  $\mu\text{m}$  band. So far, as we use only one wave band and cannot measure cloud temperature, the 10  $\mu\text{m}$  band is better for estimating cloud



FIG. 2.—Outdoor part of the MAGNUM infrared cloud monitor. Shown from top to bottom are the secondary mirror, primary mirror, and aluminum pipe housing that contains the thermal imager, signal converter, shutter controller, etc. The three rectangular plates extending from the upper edge of the housing are rain sensors that form a different system from the cloud monitor but share power and wiring.

emissivity. This is because this wavelength is around the flat-top part of the blackbody radiation of the clouds and the ground, and flux from the clouds in this band is less dependent on temperature than in the 3 ~ 5  $\mu\text{m}$  band.

We use an Amber Sentinel camera commercially produced by Raytheon in 1997. This imager has an uncooled bolometer array of 320 × 240 pixels for its detector and is sensitive enough to detect thin cirrus clouds in thermal infrared. It outputs both a standard NTSC analog signal and 12 bit digital signals at a frame rate of 30 Hz. The specifications of the imager are tabulated in Table 2.

The camera has an automatically offset flat-fielding function. It compensates for pixel-to-pixel scatter of bias and dark current signals that depend heavily on the temperature of the imager. This calibration is necessary for a quick look at raw images and is recommended every several minutes; it can be triggered by PC through an RS-232C interface. However, we do this calibration less frequently, and instead take integrated images

<sup>8</sup> GIF images of the whole-sky emissivity cloud maps can be found at <http://banana.ifa.hawaii.edu/cloud>.



FIG. 3.—Infrared cloud monitor (near the center of the image, on the roof of the container) at MAGNUM Observatory. [See the electronic edition of *PASP* for a color version of this figure.]

of a closed shutter plate for more precise compensation (see § 3.1).

Several cautions are in order here. Some imagers cannot not take clear images in a cold environment, since their detector outputs are reduced outside the operational range. Generally, outputs of uncooled bolometers change significantly with a large change in thermal background, because they are surrounded by internal parts kept at an ambient temperature. Imagers that are optimized for use at room temperature have relatively narrow operational ranges and sometimes have problems in a low-temperature environment. Our imager displayed this defect in winter in Japan and at the Haleakala site, so we asked the company to tune the electric circuit of the imager to

perform in colder environments. Moreover, we resistively heated the imager up to about room temperature at night to increase the thermal background signal from the imager itself.

Incidentally, the imager cost as much as \$40,000 when we developed our cloud monitor. Recently, products with various specifications have been made available by many manufacturers at lower costs.

## 2.2. Reflecting Optics

### 2.2.1. Design of Optics

The Cassegrain-like reflecting optics is another key component of our infrared cloud monitor. The camera's field of

TABLE 1  
SPECIFICATIONS OF MAGNUM INFRARED CLOUD MONITOR

Parameter	Value
Wavelength .....	8–14 $\mu\text{m}$
Optics .....	Thermal imager and two aspherical reflective mirrors with Cassegrain-like alignment
Sensor .....	Microthermal bolometer array of $320 \times 240$ pixels
Field of view .....	Circular field of $11^\circ$ – $70^\circ$ at zenith angle
Pixel scale .....	$0.5^\circ \text{ pixel}^{-1}$
Sampling rate .....	1 or 2 minute interval <sup>a</sup>
Sensitivity .....	$\epsilon \sim 0.015$ for blackbody temperature of 240 K

<sup>a</sup> One image is integrated for 150 frames (total of 5 s).

TABLE 2  
SPECIFICATIONS OF THE INFRARED IMAGER (AMBER SENTINEL CAMERA)

Parameter	Value
Detector	Uncooled microbolometer array
Format	320 × 240 pixels
Wavelength	8–14 μm
Lens	$f = 50$ mm, $F/0.7 \rightarrow \sim F/1.4^a$
Field of view	18° × 14°
NEDT <sup>b</sup>	<0.07 K for blackbody temperature around 25°C
Analog output	NTSC
Digital output	12 bit parallel (TTL standard signals)
Remote control	RS-232C interface
Frame rate	30 Hz

<sup>a</sup> The lens was stopped down to about  $F/1.4$  by a mask in order to improve the image quality of the reflecting optics.

<sup>b</sup> Noise equivalent differential temperature.

view is not large enough to cover the whole sky and must be expanded by other optics. Germanium crystal is generally used for the lenses of these thermal imagers, because it is very transparent in thermal infrared. However, fish-eye lenses made of this material are not commercially available and are also hard to develop or fabricate without a great deal of expenditure. Thus, it is reasonable to use some kind of convex mirror system.

For the fundamental shape of the mirrors, we based ours on the particular aspherical mirrors introduced by Chahl & Srinivasan (1997). When we look into these types of mirrors along their optical axis, the appearance of the reflected field is not radially deformed; they preserve a linear relationship between the apparent angle from the image center and the real radial angle from the field center. A simple spherical mirror produces a radially compressed image toward the image edge; the more distant from the image center we see objects through the mirror, the more radially compressed they appear.

We align the camera with the surface of a mirror, using polar coordinates as shown in Figure 4, where the lens node of the imager is located at the origin  $O$ , and the mirror surface is adjusted by the revolution of the function  $r(\theta)$  around the  $Z$ -axis. Here  $\theta$  is an angle of line of sight with the  $Z$ -axis in the camera field, and  $\Theta$  is a line-of-sight angle with the  $Z$ -axis in the negative direction in the real field that is seen through both the camera and the mirror. According to Chahl & Srinivasan (1997),  $\Theta$  proportionally corresponds to  $\theta$  if  $r(\theta)$  is given by

$$r(\theta) = \frac{r_0(\sin \gamma_0)^{-1/\kappa}}{[\sin(\kappa\theta + \gamma_0)]^{-1/\kappa}}, \quad (1)$$

where  $r_0$  is the distance between the mirror and  $O$  along the  $Z$ -axis,  $\gamma_0 = \tan^{-1} [dr(\theta = 0)/dz]$  is the initial angle of the mirror (i.e., half of the vertex angle), and  $\kappa$  relates to the proportionality constant  $\alpha$  between  $\theta$  and  $\Theta$  (which is field-widening power) as

$$\frac{d\Theta}{d\theta} = -1 - 2\kappa = \alpha. \quad (2)$$

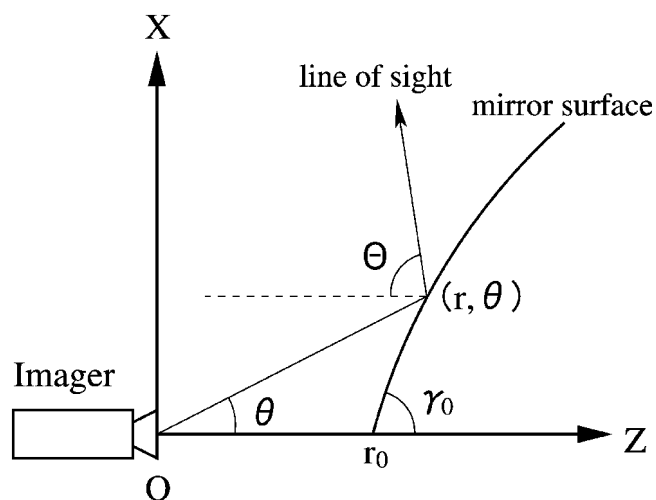


FIG. 4.—Basic alignment of the imager and diagram of the panoramic aspherical mirror surface introduced by Chahl & Srinivasan (1997).

If we place the mirror with the convex side upward and direct the camera to look down on the mirror vertically, we can see the sky at zenith angle between  $\Theta_{\min}$  and  $\Theta_{\max}$  in degrees:

$$\Theta_{\min} = 2(90^\circ - \gamma_0) \quad (3)$$

and

$$\Theta_{\max} = \theta_{\max} + 2 \left\{ 90^\circ - \tan^{-1} \left[ \frac{dr(\theta = \theta_{\max})}{dz} \right] \right\}. \quad (4)$$

A circular image of the whole sky is obtained by setting  $\theta_{\max}$  as half the shorter angle of the rectangular field of view of the imager.

Chahl & Srinivasan (1997) also suggested a two-mirror system with Cassegrain-like alignment in which the aspherical shape introduced above is used as a primary mirror, and a conelike shape is used as secondary, as shown in Figure 5. Here the secondary with half a vertex angle of  $\beta$  is placed with its surface facing the imager, which is equivalent to the configuration in Figure 4, with  $\gamma_0 = \beta$ . The section of its surface is triangular, equivalent to  $\alpha = 1$ , which means the surface has no field-widening power. The section of primary mirror surface should be drawn similarly to that in Figure 4, but using an  $X'O'Z'$  coordinate system in which  $O'$  is symmetrical with  $O$  about the section of the secondary surface. If  $\beta$ ,  $r'_0$ , and  $\gamma'_0$  are properly optimized, the light coming from the zenith ( $\theta = \Theta = 0$ ) can reach the imager, avoiding the secondary mirror by way of  $r'_0$  and the secondary vertex. Then the entire sky, including the zenith, can be seen.

However, although the idea is very attractive, we found a serious astigmatic aberration in these optics that is mostly derived from the conical shape of the secondary. When seen from above along the optical axis, there is no curvature along the

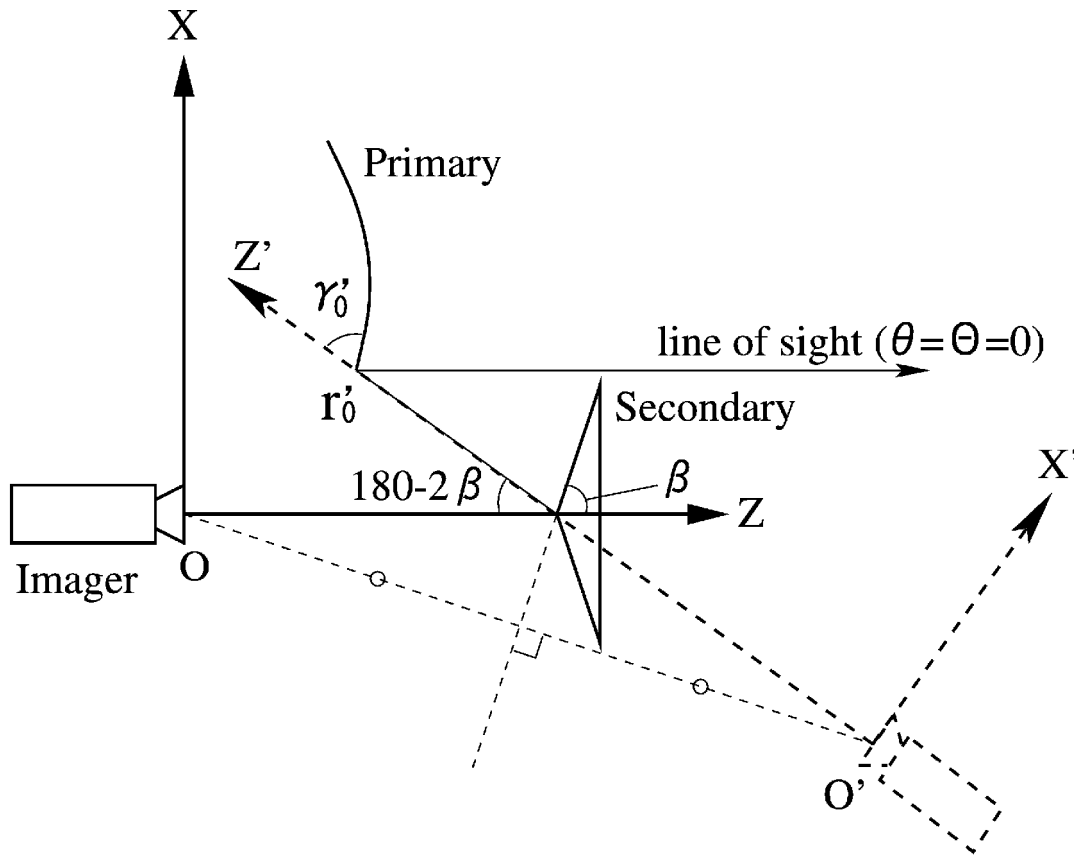


FIG. 5.—Basic alignment of the imager and diagram of the Cassegrain-like mirror system that was originally introduced.

sagittal directions on the completely cone-shaped surface, whereas curvature exists tangentially. This aberration becomes extremely large if we use an imager with a large lens aperture. The combination of our 71 mm aperture lens imager and 240 mm diameter primary mirror, which was restricted by our manufacturing capacity, results in a point-spread function (PSF) size of over 1 mm on the detector, which corresponds to  $10^\circ$  in the sky.

We therefore did not completely follow the original two-mirror system scheme, and instead improved it to upgrade image quality at the cost of viewing near zenith and some amount of sensitivity. In particular, we significantly flattened the vertex angle of the cone-shaped secondary mirror to reduce its tan-

gential curvature. Next, we introduced an aspherical shape similar to that of the secondary mirror in Figure 4, so that it also has a field-widening power to some extent, similar to a primary mirror. In fact,  $O'$  projected by the section of this type of secondary surface does not strictly converge at one point, but it was found that its effect on the field deformation could be ignored. Moreover, we adopted a smaller primary-mirror hole to reduce the shadow area in the image center, and also to extend the focal depth. Because the primary hole forces a reduction in the imager's lens aperture, the decline in sensitivity is compensated for by frame integration.

As a result of these improvements, we adopted the parameters listed for the "Improved" model in Table 3. The param-

TABLE 3  
DESIGN PARAMETERS OF ORIGINAL VS. IMPROVED SYSTEMS

MODEL	PRIMARY						SECONDARY			
	$O'(X, Z)^a$ (mm)	$r'_0$ (mm)	$\gamma'_0$ (deg)	$\alpha$	$\phi_{out}^b$ (mm)	$\phi_{in}^c$ (mm)	$r_0$ (mm)	$\gamma_0$ (deg)	$\alpha$	$\phi_{out}^b$ (mm)
Original .....	(-52, 595)	530	85.0	11.0	240	80	300	85.0	1.0	80
Improved .....	(-2, 488)	360	89.6	4.4	240	38	340	89.6	2.3	100

<sup>a</sup> The position of the virtual node  $O'$  for the primary in the coordinates  $XOZ$ .

<sup>b</sup> Outer diameter.

<sup>c</sup> Inner diameter; that is, the diameter of the center hole of the primary.

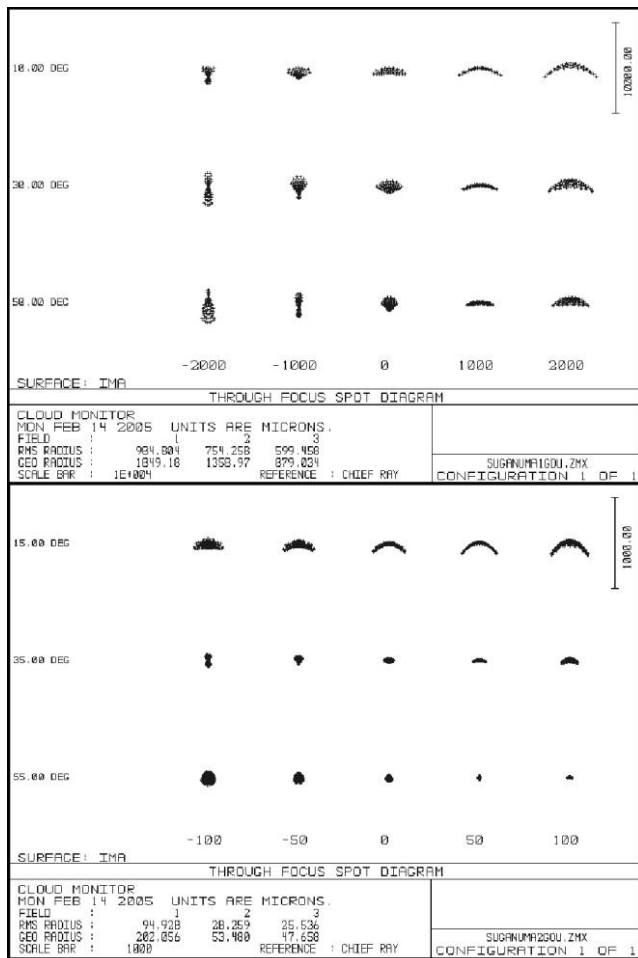


Fig. 6.—*Top*: Spot diagram through the focus using the “Original” model of the mirror system optimized to our camera, following Chahl & Srinivasan (1997). *Bottom*: Similar diagram for the “Improved” model. Note that the unit of scale for the spots is a micron, and the scale bar in the top panel is 10 times larger than that in the bottom. The pixel scale of the imager detector is 50  $\mu\text{m}$ .

eters that were determined following the original plan in Figure 5 are also listed for reference as “Original.” Our “Improved” model gives a shadow circle with a radius of  $11^\circ$  at the zenith. However, the area is not critical for us because the MAGNUM telescope rarely observes objects around the zenith, because of the sparse distribution of celestial coordinates of our targets and because of some operational restrictions of our telescope.

Most remarkable is that the image resolution was dramatically increased in our “Improved” model. Figure 6 shows spot diagrams of ray-traced images for both the “Original” and “Improved” models. The specifications of the two models are also tabulated in Table 4. The “Improved” model decreases the size of the PSFs by an order of magnitude or more. There remains some astigmatism and field curvature in our “Improved” model, but the PSF size is within a few pixels over almost the entire field of view.

TABLE 4  
SPECIFICATIONS OF ORIGINAL AND IMPROVED MIRROR SYSTEM

MODEL	RMS SIZE OF PSF		FOV <sup>a</sup> (deg)	FOCAL RATIO
	( $\mu\text{m}$ )	(pixels)		
Original	600–1000	12–20	0–70	$F/0.7$
Improved	26–95	0.5–2	11–70	$F/1.4$

<sup>a</sup> Measured in zenith angle.

### 2.2.2. Fabrication and Construction of Mirror System

The surfaces of the mirrors were shaped by diamond-turning on brass that is easily worked and goes well with gold coating. Using an ultraprecise computerized, numerically controlled (CNC) turning machine, we obtained a surface roughness of about 20 nm in rms, which is sufficient for a mirror at a wavelength of 10  $\mu\text{m}$ . The surface was plated with solid gold containing 5% cobalt, with a thickness of 2  $\mu\text{m}$ . Finally, a physical vapor sapphire was deposited on the surface at a thickness of 0.2  $\mu\text{m}$  for protection. The surface reflectivity is about 95%, and no serious degradation has been seen in 5 years of outdoor operation.

On the first attempt to process the mirror surface, we tried an aluminum-based alloy plated with electroless nickel and coated with gold on the surface. However, we found that the gold coat degraded in a few months’ exposure to air. The pinholes in the nickel plating might also cause water to rapidly erode the aluminum base.

On the central hole of the primary mirror was placed a chemical-vapor-deposited (CVD) diamond plate with a thickness of 0.2 mm and transparency of about 80% at  $\lambda \sim 10 \mu\text{m}$  with no coat. A germanium plate processed with antireflection coating on both the top and bottom, and protective coating on the top, could also work in some environments and has been used in similar systems at several sites, such as Mauna Kea in Hawaii and Atacama in Chile. However, during our test operation in Tokyo, Japan, the upper surface of the germanium window degraded in a few months. We suspect that rain in Tokyo is very acidic, which might enhance degradation of the protective coating.

### 2.3. Data Acquisition System

The thermal imager, the Amber Sentinel camera, outputs images with standard NTSC analog signals as well as 12 bit parallel-channel digital signals at a rate of 30 frames  $\text{s}^{-1}$ . We use the digital output because an 8 bit analog signal loses the lower 4 bits of original signal, which is much larger than the noise signal of 1 or 2 ADU (analog-to-digital units) and is difficult to restore by frame integration afterward.

For each data bit, together with synchronizing clocks for frame acquisition, the digital signals are single-ended transistor-transistor-logic (TTL) standards. We convert these signals to differential RS-422 standard level signals using a hand-made digital electrical circuit with integrated circuits in order to transmit the signals to a PC about 15 m away

from the outdoor system. This is because the TTL signals are too delicate to send more than several tens of centimeters at a high data rate in a noisy environment.

The signals are acquired by a Linux PC using a digital frame-grabber board (PC-DIG, produced by Coreco, Inc.). It can grab digital data from 12 parallel channels at the rate of 4.6 Mbytes  $s^{-1}$  for our imager, and its driver for Linux OS is supported by the company.

We integrate the images for 5 s, corresponding to 150 frames, to increase the signal-to-noise ratio. Integration for more than 10 s is not favorable, because whole-sky images of clouds are often blurred by migrations of clouds.

For each acquisition of the whole-sky image, we take shutter images immediately before and after it. In addition, the temperature of the blackbody reference plate is measured at the same time.

The data sets are acquired about every 1 or 2 minutes while the elevation of the Sun is below  $15^\circ$ . We cease operation almost entirely during the daytime, in case direct rays of sunlight degrade the imager detector.

### 3. ANALYSIS SOFTWARE

#### 3.1. Data Reduction

Each whole-sky image is processed immediately after acquisition of the shutter images, the blackbody reference temperature, and some calibration data measured in advance. Figure 7 illustrates how we reduce a raw whole-sky image into the apparent emissivity map of the clouds.

First, offset flat-fielding for the pixel-to-pixel pattern is done by subtracting the average of the two shutter images obtained before and after the incident exposure of the whole-sky image. The automatic offset flat-fielding by the camera is convenient for snapshot images but is not sufficient for our frame-integrated whole-sky images. We can perform a similar calibration with a higher signal-to-noise ratio using the frame-integrated shutter images.

Next, background signals from the optics and the interior of the imager are subtracted. There are two types of components of background signal: flat-offset components and spatial-pattern components. These differ from each other with varying internal and environmental temperatures and have to be subtracted separately.

The flat-offset background component includes bias and dark current signals of the detector, along with thermal radiation from the interior of the imager and the optics, which should be compensated for with each whole-sky image. Only the subtraction of the shutter image from the whole-sky image does not work well, because the surface brightness of the shutter and the thermal background from the optics vary independently. The flat-offset value of the background signal,  $C_{\text{off}}$ , on the whole-sky image is calculated from the temperature of the blackbody reference plate,  $T_{\text{ref}}$ , and its signal,  $C_{\text{ref}}$ , on the in-

cident whole-sky image as

$$C_{\text{off}} = C_{\text{ref}} - \frac{1}{g} \int B_{\lambda}(T_{\text{ref}}) d\lambda, \quad (5)$$

where  $B_{\lambda}(T_{\text{ref}})$  is the Planck function for temperature  $T_{\text{ref}}$ , and  $g$  is the signal-to-surface brightness ratio measured beforehand. The units of  $C_{\text{off}}$  and  $C_{\text{ref}}$  are ADU. We subtract the single value of  $C_{\text{off}}$  from each pixel in the incident whole-sky image.

There remains a spatial-pattern background component that mainly originates in the baffle of the reflecting optics and the atmosphere. The pattern of this type of background is radially symmetrical and is almost stable on clear nights. We therefore prepare beforehand a template whole-sky image for a clear night. The template image should be acquired when the sky is certain to be clear, and reduced up to compensating for the flat-offset background. We subtract the template image from all whole-sky images.

Once the background signals have been subtracted, we convert the signals in the whole-sky image into a surface-brightness value using the signal-to-surface brightness ratio  $g$ . One can determine the value of  $g$  in the laboratory by exposing blackbody targets of different temperatures, or it can be determined at the observatory by simultaneously exposing both a clear sky and a black object of ambient temperature. Note that the value of  $g$  is dependent on zenith angle, mainly because of vignetting on the aperture of the camera lens. We should therefore measure  $g$  for several zenith angles, and using a function fitted to them. Figure 8 shows the data for  $g$  measured for our system at the MAGNUM Observatory site.

Finally, the surface brightness  $S$  in the image is converted to the apparent emissivity  $\epsilon$  of the clouds at a  $10 \mu\text{m}$  wave band, which is related to  $S$  as

$$S = \epsilon \int B_{\lambda}(T_c) d\lambda, \quad (6)$$

where  $B_{\lambda}(T_c)$  is the Planck function for the cloud temperature  $T_c$ . According to the average annual air temperature of 296 K at sea level in Maui Island, combined with a lapse rate of  $-6.5 \text{ K km}^{-1}$  for the standard atmosphere (Committee on Extensions to the Standard Atmosphere 1976), the expected ambient temperature at an altitude of 10,000 m above Haleakala Observatory should be about 240 K. We therefore calculate  $\epsilon$  assuming (hereafter fixing) the temperature of  $T_c = 240 \text{ K}$  to be representative of high-altitude clouds or cirrus.

Note that  $\epsilon$  includes the reflection efficiency of a cloud as well as the absorption efficiency, and in  $S$ , there is a significant amount of reflected emission by the cloud that originates on the surface of the ground or sea. This means we cannot simply convert the apparent emissivity  $\epsilon$  to optical depth, which relates to actual absorption efficiency. However, it is reported that for high-altitude clouds in particular, a large amount of emission

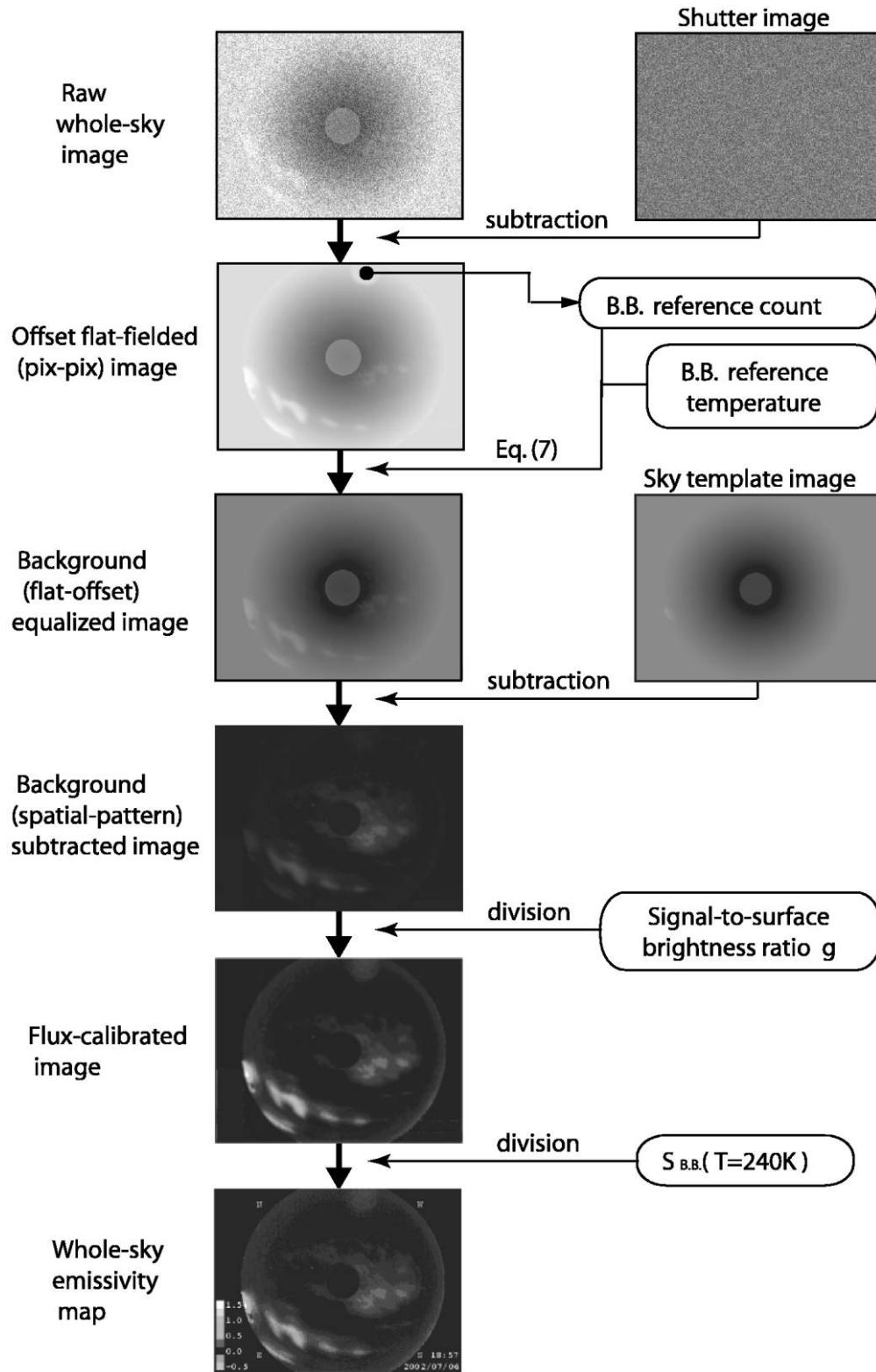


FIG. 7.—Block diagram of the reduction from a raw whole-sky image into a whole-sky cloud emissivity map.

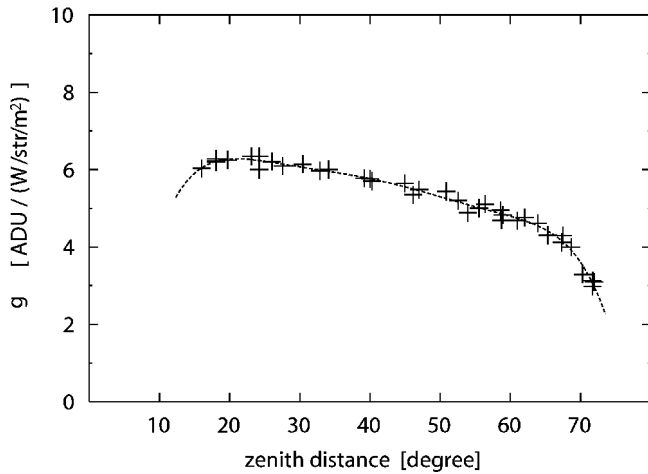


FIG. 8.—Signal-to-surface brightness ratio  $g$  of the MAGNUM infrared cloud monitor system, measured as a function of zenith angle. The dashed line is a fit to the measured points and is used for  $g$  in Fig. 7 and eq. (5).

still originates thermally in the clouds themselves (Platt & Stephens 1980). Figure 9 shows whole-sky cloud emissivity maps obtained and processed under various sky conditions.

It is very convenient for a remote observer in Japan or even at the Haleakala site to see the whole-sky cloud emissivity maps on the Internet. However, our main objective in operating the MAGNUM observatory is automated observation using real-time consideration of weather conditions. We therefore developed software that can detect clouds from the whole-sky cloud emissivity maps and evaluate observational conditions from them (§ 3.2 and § 3.3).

### 3.2. Automatic Cloud Detection

To determine whether clouds exist or not in a certain part of the sky, it is important to measure both the average and the standard deviation values of emissivity in a small area in approximately that direction, rather than to refer to just one pixel value. Here two elements limit sensitivity: one is variation in the zero emissivity level caused by a residual thermal background signal, and the other is pixel-to-pixel noise. The empirical value of the former for our system is about  $\epsilon = 0.25$ , which is considerably larger than for thin clouds. This mainly comes from the residual pattern of the background radiation, which is difficult to subtract completely from a single-template whole-sky image. In addition, there is a correlation of humidity with residual background.

The limit for the pixel-to-pixel sensitivity is about  $\epsilon = 0.015$  as a noise equivalent signal of the image, which is much less than the limit due to residual thermal background. Thin clouds are easy to detect by their spatial fluctuations of emissivity rather than by emissivity values themselves.

We therefore divide a whole-sky cloud emissivity map into 90 subareas, each of which is  $10^\circ$  in elevation and  $20^\circ$  in

azimuth. For each subarea, we categorize the cloud condition into one of several levels using the average emissivity  $\bar{\epsilon}$  and the rms emissivity  $\sigma(\epsilon)$  calculated for the area.

Figure 10 shows the  $\sigma$  versus  $\epsilon$  diagram on which each subarea can be evaluated. A subarea is evaluated as being “clear” only when both  $\bar{\epsilon} < 0.25$  and  $\sigma(\epsilon) < 0.05$ ; otherwise, it is regarded as being covered by some clouds. A subarea that is not labeled “clear” is divided into “thin,” “thick,” or “rain” when  $\bar{\epsilon} < 0.4$ ,  $0.4 \leq \bar{\epsilon} < 1.5$ , or  $\bar{\epsilon} \geq 1.5$ , respectively. The condition of “rain” means that the surface brightness is as large as for a blackbody for atmospheric temperature at the Haleakala summit, and that the mirror system is possibly wet due to rainfall or moisture, although the direct detection of rainfall should be performed by rain sensors. Each subarea is given a value of 0 for “clear,” 1 for “thin,” 2 for “thick,” or 3 for “rain” in order to calculate whole-sky cloud conditions from statistics over all subareas (see § 3.3).

The main cause preventing detection of even thinner clouds is the residual pattern of the thermal background on the whole-sky emissivity maps, which increases the rms value of emissivities, even in a small subarea. This could be improved if a relation between the radial pattern and the temperature of the reflecting optics is established, or if the temperature of the reflecting optics is regulated. More fundamentally, we are soon going to improve the design of the reflecting optics so that there will be no vignetting of objects in the optical pass.

### 3.3. Classification of Whole-Sky Cloud Condition

To determine whether the sky will allow observations and what type of observation is best to execute, we evaluate the whole-sky cloud condition using statistics over subarea values calculated and labeled in § 3.2. We classify the whole-sky cloud condition into five types: CLEAR, THIN-or-PARTIAL, MEDIUM, CLOUDY, and RAINY.

First, for safety, we strictly exclude conditions in which there are many subareas of “rain.” Figure 11 shows the classifications of whole-sky cloud conditions on average over subarea values versus a “rain” subarea coverage plane. When the “rain” subarea coverage is larger than 10%, the whole-sky condition is evaluated as being either MEDIUM, CLOUDY, or RAINY, and we do not start any type of observation.

When the “rain” subarea coverage is less than 10%, we classify whole-sky cloud conditions into five types, as given in Figure 12. Here cloud coverage includes both “thin” and “thick” subareas. The whole-sky cloud condition is evaluated as being CLEAR only at the origin of Figure 12, which means all subareas are “clear.” With the exception of CLEAR, whole-sky cloud conditions are classified as either THIN-or-PARTIAL, MEDIUM, or CLOUDY, according to the cloud coverage and mean subarea level.

The classifications above have mainly been working successfully, although they are empirical and somewhat inelegant.

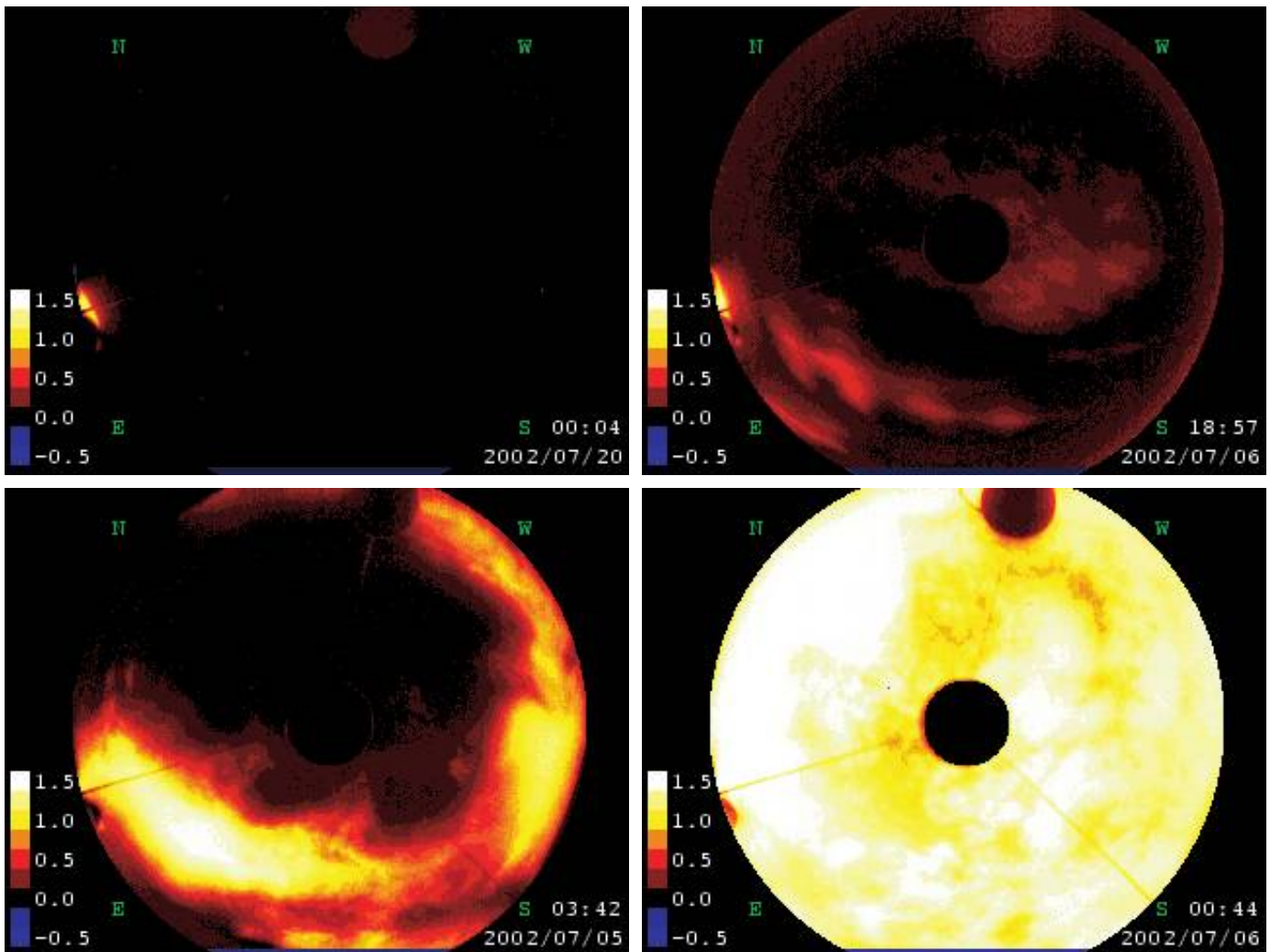


FIG. 9.—Whole-sky cloud emissivity maps acquired and processed by the MAGNUM infrared cloud monitor under various sky conditions: clear (*top left*), thin (*top right*), partially cloudy (*bottom left*), and entirely cloudy (*bottom right*). There are two shadow circles in each image: the small one at the image center is field vignetting from the hole of the primary and secondary mirrors, and the circle near the edge of the image is a blackbody reference plate.

#### 4. PERFORMANCE

##### 4.1. Automated Observation with Infrared Cloud Monitor at MAGNUM Observatory

Our cloud monitor was located at the Haleakala site and began to produce whole-sky cloud emissivity maps when the MAGNUM observatory started its telescope operation in 2000 August. Automated monitoring observations of active galaxies, while employing the cloud monitor, were then put into practice in early 2001. After several months of refinements, we were able to achieve fully automated astronomical observations for an entire night. Now we have continuous unmanned observation, with maintenance being carried out every several months (Kobayashi et al. 2003, 2004)

According to the whole-sky cloud condition evaluated by the cloud monitor, our automated observing system decides whether or not observations are possible. When the whole-sky cloud condition is either CLEAR or THIN-or-PARTIAL, the observing system opens the dome slit and commences observation. When the whole-sky cloud condition is CLOUDY or RAINY, the observing system closes the dome slit and does not carry out observations. When the whole-sky cloud condition is MEDIUM, the observing system maintains the on-going operation.

We also use the whole-sky cloud condition to determine what type of observation should be executed. If the condition is CLEAR, which can be regarded as a photometric sky, all types

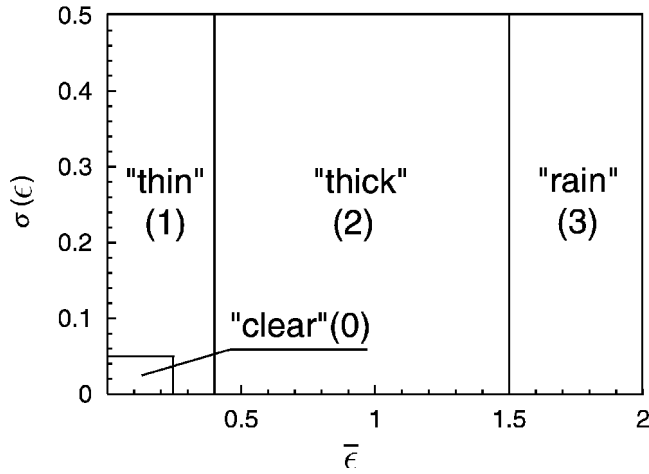


FIG. 10.—Classification of cloud status for each subarea of  $20^\circ$  (azimuth)  $\times$   $10^\circ$  (elevation) from its average emissivity  $\bar{\epsilon}$  and standard deviation  $\sigma(\epsilon)$ . A numerical value in parentheses in each zone indicates a level for calculating whole-sky cloud conditions (see § 3.3).

of observations are possible. If the condition is THIN-or-PARTIAL, certain observations that are sensitive to cloud extinction are restricted; for instance, observations such as standard-star calibration, relative photometry between several separate fields, or imaging of faint objects are allowed only in CLEAR conditions. Instead, differential photometry between the bright objects in the same field of view is permitted in THIN-or-PARTIAL conditions, because this is barely affected by extinction fluctuations.

The whole-sky cloud condition and status of the subarea in which the telescope is pointing are recorded in the FITS header of observed images. The whole-sky emissivity maps are also archived so that we can check the quality of the observed astronomical data when we analyze them.

Operation of the cloud monitor has mainly been stable since 2000, except in the first half of 2002, when we experienced several months of trouble with the frame-grabber board. Regular maintenance includes wiping dust from the mirror and shipping whole-sky images to Japan when we visit the site every several months.

In the following two sections (§ 4.2 and § 4.3), we present and discuss the performance of our cloud monitor, comparing it with other weather sensors and photometric data.

#### 4.2. Conservative Warning for Rainfall

The most basic function required of our cloud monitor is to determine whether or not the sky allows observations. When the sky becomes cloudy, the cloud monitor should close the dome slit before rain falls. It should also stop useless and risky opening of the dome when the sky is still covered by thick clouds.

Table 5 shows the frequency distribution of various weather

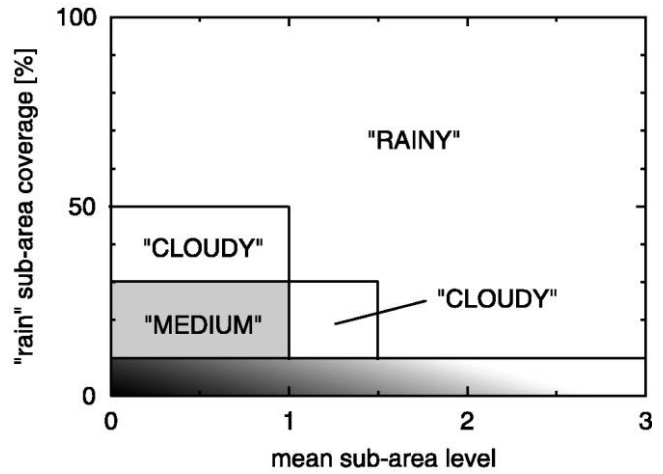


FIG. 11.—Classification of whole-sky cloud conditions from “rain” subarea coverage vs. mean subarea level over all areas. The zone on the bottom with tonal gradation, representing “rain” subarea coverage below 10%, is classified into several conditions in Fig. 12.

conditions over 4 years from two different weather-sensing systems, including the whole-sky cloud monitor and the rain sensor. Note that the rain sensor directly senses raindrops by means of changes in the resistivity of the electrical circuit, while the cloud monitor only inspects the surface brightness of the sky image. The percentages of rain-sensor output at night are 85.8% for “DRY” and 14.2% for “RAIN.”

Table 5 indicates that a combination of CLOUDY and RAINY comprises 96% of RAIN; i.e., raindrops can be avoided by the high probability of rain from such a combined cloud condition. The remaining 4% probability corresponds to a sit-

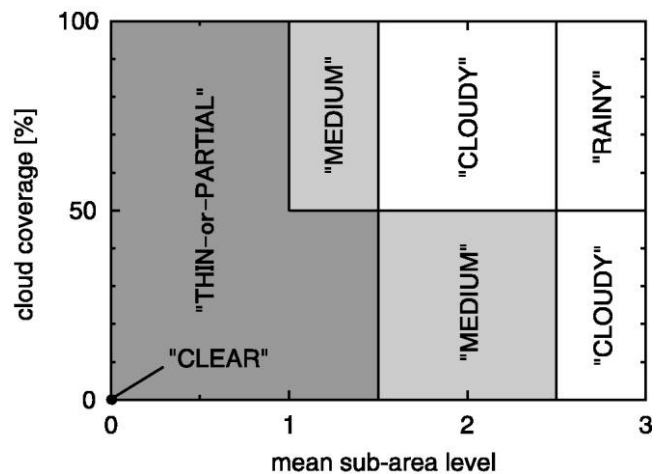


FIG. 12.—Classification of whole-sky cloud conditions from cloud coverage vs. mean subarea level over all areas. This classification is applied only when “rain” subarea coverage is below 10%. The cloud coverage includes both “thin” and “thick” subareas. Only the origin of the diagram, where all the subareas are “clear,” is the coverage indicated as being CLEAR.

TABLE 5  
CORRELATED CLASSIFICATIONS FROM TWO DIFFERENT  
WEATHER SYSTEMS

RAIN SENSOR	CLOUD MONITOR					TOTAL
	CLR	THN	MED	CDY	RNY	
DRY .....	55.8	18.0	2.5	5.9	3.5	85.8
RAIN .....	0.1	0.4	0.2	0.7	12.9	14.2
Total (%) .....	55.9	18.4	2.7	6.6	16.4	100.0

NOTES.—CLR, THN, MED, CDY, and RNY mean the whole-sky cloud conditions CLEAR, THIN-or-PARTIAL, MEDIUM, CLOUDY, and RAINY, respectively. Note that the rain sensor directly senses rain drops or thick moisture, while the RAINY condition indicated by the cloud monitor means that there are high-emissivity regions at the 10  $\mu\text{m}$  wave band in the field of view.

uation in which the rain sensor catches raindrops while the output from the cloud monitor is CLEAR, THIN-or-PARTIAL, or MEDIUM. It would decrease further if acquisition of whole-sky data were carried out more frequently, because the approach of moisture is sometimes very rapid. However, the humidity sensor usually helps to identify the moisture on its way to the observatory.

#### 4.3. Determination of Whether the Sky is Photometric

The next important function required of the cloud monitor is to determine whether or not the night is photometric. The flux calibration of active galaxies using reference stars or standard stars in different telescope directions often fails if we are uncertain whether the sky is entirely clear. Reliability of the whole-sky condition CLEAR can be estimated from statistics of accumulated standard star flux data, because these have been observed quickly while the whole-sky was CLEAR.

Table 6 presents several statistical values of our standard-star observations over 2 years while the instrumental throughput was relatively stable. Columns (1) and (2) are the wave band and effective wavelength, respectively. Column (3) is the number of observations. The standard deviation of the fluxes over all observations  $\sigma_{\text{all}}$  for each band is given in column (4), and the average over individual photometric errors  $\langle \text{err} \rangle$  is given in column (5). Nominal extinction values for units of air mass  $Q_{\text{atm}}$ , measured by intensive observations of standard stars on a few nights, are shown in column (6). The linear trend of flux decreasing with time during the observing period, derived from changes in telescope throughput, has been corrected. Air-mass correction for elevation in each observation is done with a constant value in the table.

The photometric errors  $\langle \text{err} \rangle$  are so small that they contribute little to  $\sigma_{\text{all}}$ . Therefore, the scatter  $\sigma_{\text{all}}$  mainly contains the day-to-day changes in extinction by the atmosphere or clouds.

Converting  $\sigma_{\text{all}}$  and  $Q_{\text{atm}}$  to a flux ratio, we show  $\Delta F/F$  against wavelength  $\lambda$  in Figure 13. The vertical bars with inverted triangles represent  $\sigma_{\text{all}}$  after correcting for  $\langle \text{err} \rangle$ . Filled squares show  $Q_{\text{atm}}$ . The solid line is a linear fit to the filled squares, except for the *K*-band, which is particularly affected by water

TABLE 6  
STATISTICS OF STANDARD-STAR OBSERVATION

Band	Wavelength	$N_{\text{obs}}^a$	$\sigma_{\text{all}}^b$	$\langle \text{err} \rangle^c$	$Q_{\text{atm}}^d$
(1)	( $\mu\text{m}$ )	(3)	(mag)	(mag)	(mag)
<i>U</i> .....	0.36	73	0.108	0.006	0.338
<i>B</i> .....	0.44	113	0.058	0.004	0.223
<i>V</i> .....	0.55	154	0.033	0.004	0.111
<i>R</i> .....	0.65	110	0.023	0.004	0.072
<i>I</i> .....	0.79	97	0.020	0.004	0.057
<i>J</i> .....	1.25	86	0.028	0.010	0.010
<i>H</i> .....	1.63	95	0.027	0.009	0.009
<i>K</i> .....	2.20	54	0.024	0.012	0.044

NOTES.—The observations are triggered only when the whole-sky condition calculated by the cloud monitor is CLEAR. Air-mass effects for elevation are corrected by  $Q_{\text{atm}}$ . Linear trends of decreasing flux during the 2 year period of observations are also corrected.

<sup>a</sup> Number of observations.

<sup>b</sup> Standard deviations of flux over observations.

<sup>c</sup> Average photometric error for each night.

<sup>d</sup> Nominal extinction value per unit air mass measured at our observatory.

vapor. The line shows the wavelength dependence of  $\Delta F/F \propto \lambda^{-2.4}$ , which is consistent with a typical trend of a mixture of Rayleigh-scattering by molecules and Mie-scattering by small aerosols in the atmosphere (Cox 2000).

A similar linear wavelength dependence is seen in  $\sigma_{\text{all}}$  in the optical and should be dominated by daily or seasonal variation in the extinction by the atmosphere. On the other hand,  $\sigma_{\text{all}}$  at longer wavelengths beyond the *R* band is near-constant, regardless of the wavelength dependence of  $Q_{\text{atm}}$ . We consider that this flat component of  $\sigma_{\text{all}}$  could include variation in ex-

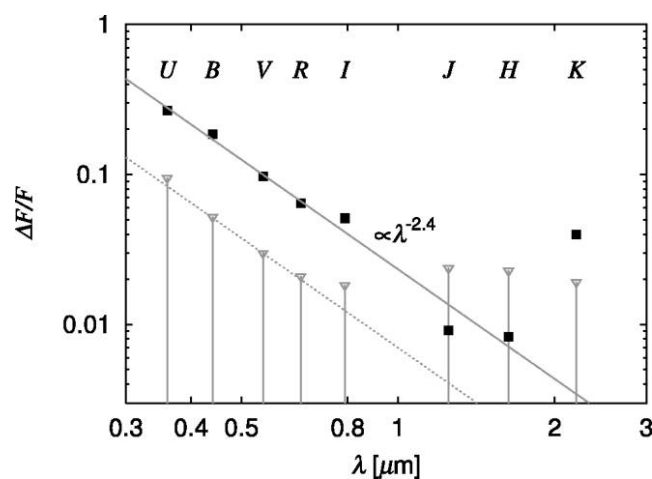


FIG. 13.—Plot of  $\sigma_{\text{all}}$  and  $Q_{\text{atm}}$  from Table 6 on wavelength vs. flux ratio plane. The inverted triangles with vertical lines represent  $\sigma_{\text{all}}$  and are correlated with  $\langle \text{err} \rangle$ . Filled squares show  $Q_{\text{atm}}$ . The line fitted to the squares, excluding the *K* band, shows the wavelength dependence of  $\lambda^{-2.4}$ . The dotted line shows a factor of 3 decrease from the fitted line.

tion by clouds missed by our cloud monitor, because the size of typical cloud particles is on the order of 10  $\mu\text{m}$ , and there is little dependence of extinction on wavelength at a few microns or less. Therefore, photometric errors caused by the extinction of clouds are restricted to within a few percent.

### 5. TREND OF WHOLE-SKY CLOUD CONDITIONS AT HALEAKALA

Bradley et al. (2006) presented an overview of meteorological characteristics at Haleakala with respect to many types of weather data, such as humidity, temperature, wind speed, and cloud coverage. However, their analysis is based on a compilation of various records with a fairly large spatial and time resolution, including some taken by satellites. Our whole-sky cloud conditions are more straightforward and systematic, because our conditions are completely based on direct measurements of clouds that appear in the sky above the observatory.

Table 7 shows the proportions of whole-sky cloud conditions averaged monthly between 2001 January and 2005 December. Data from several readings in early 2001 are combined from test operations of analysis software. A total of 668,063 whole-sky images for 1601 nights are used to provide the statistics in the table.

Figure 14 presents the relative frequencies of the whole-sky cloud conditions combined over the data in Table 7. The percentage of each condition is an average over the data, weighted by the number of nights in which the data were obtained. The monthly percentage for combined conditions between 2001 January and July is divided into respective conditions, according to their average proportions after 2001 August.

It should be noted that despite CLEAR and THIN-or-PARTIAL conditions, observations were sometimes impossible, due to other weather warnings, such as high humidity and strong wind. Moreover, observations were not carried out when the wet sensor warned that the dome was not dried out after rainfall or moisture. At Haleakala, more than 50%–60% of all night time is near-photometric, and about 75% of the time, it is feasible to execute particular observations. This observable sky frequency is comparable to that of Mauna Kea.<sup>9</sup> Add to this its good access, and Haleakala is therefore one of the best locations for optical and near-infrared observations in the Northern Hemisphere.

Next, Figure 15 shows the monthly average relative frequency of the whole-sky cloud condition. Clear seasonal cycles over a year can be seen; there are high observable rates in summer and winter, and low rates in early spring and late autumn, in agreement with Bradley et al. (2006). It has generally been said that there is a dry summer season and rainy winter season in Hawaii. However, our data demonstrate that the sky conditions in midwinter are not very bad at Haleakala.

TABLE 7  
MONTHLY AVERAGE OF WHOLE-SKY CLOUD NIGHT CONDITIONS

Year	Month	Number						
		of Nights	$N_{\text{data}}$	CLR	THN	MED	CDY	RNY
2001	Jan	20	6981		90.4 <sup>a</sup>		3.6	6.0
	Feb	14	5121		68.3 <sup>a</sup>		5.7	26.0
	Mar	31	11,097	83.0 <sup>b</sup>		2.3	2.6	12.1
	Apr	28	8946	62.5 <sup>b</sup>		5.5	6.3	25.7
	May	31	11,732	93.6 <sup>b</sup>		1.9	0.8	3.7
	Jun	30	12,351	65.9 <sup>b</sup>		9.5	10.3	14.3
	Jul	31	12,328	62.8 <sup>b</sup>		12.3	10.4	14.5
	Aug	31	13,051	67.0	25.3	2.4	2.7	2.6
	Sep	30	13,210	55.1	25.1	3.1	8.8	7.9
	Oct	31	14,540	47.1	22.7	2.4	8.8	19.0
	Nov	30	14,424	46.9	22.9	2.1	9.4	18.7
	Dec	7	3427	0.0	76.3	3.6	10.5	9.6
2002	Jan	0	0	...	...	...	...	...
	Feb	0	0	...	...	...	...	...
	Mar	0	0	...	...	...	...	...
	Apr	0	0	...	...	...	...	...
	May	0	0	...	...	...	...	...
	Jun	10	3021	18.3	71.2	3.6	4.9	2.0
	Jul	31	11,703	59.8	19.2	4.3	9.0	7.7
	Aug	31	9792	33.3	28.0	5.9	15.6	17.2
	Sep	30	9071	60.0	20.9	3.4	7.7	8.0
	Oct	31	9777	42.9	19.3	6.3	8.8	22.7
	Nov	30	12,246	70.3	20.5	1.5	4.9	2.8
	Dec	31	14,665	79.7	8.4	0.7	1.5	9.7
2003	Jan	31	14,500	73.6	11.4	2.0	2.4	10.6
	Feb	28	12,611	80.8	6.1	0.7	3.6	8.8
	Mar	31	13,318	67.6	11.0	1.4	4.9	15.1
	Apr	30	12,291	37.0	35.6	3.9	6.7	16.8
	May	27	10,326	54.6	28.7	6.6	9.8	0.3
	Jun	30	11,761	64.9	22.9	1.4	4.6	6.2
	Jul	31	12,212	55.6	19.7	3.8	8.9	12.0
	Aug	31	12,025	48.9	24.4	9.0	6.1	11.6
	Sep	29	11,754	82.2	11.6	0.8	2.6	2.8
	Oct	31	13,856	43.9	27.6	4.0	11.6	12.9
	Nov	30	13,992	53.3	20.0	4.3	6.3	16.1
	Dec	31	14,755	55.5	8.7	2.3	4.4	29.1
2004	Jan	31	14,590	52.8	10.6	2.1	5.5	29.0
	Feb	29	13,095	62.4	11.2	1.7	9.0	15.7
	Mar	31	13,338	20.6	17.3	2.8	17.0	42.3
	Apr	30	12,444	50.5	12.8	2.5	5.8	28.4
	May	31	12,569	39.1	15.1	3.4	9.5	32.9
	Jun	30	11,991	52.5	24.4	3.0	9.8	10.3
	Jul	31	12,490	80.0	9.7	1.1	3.3	5.9
	Aug	31	12,837	64.9	13.9	1.3	2.3	17.6
	Sep	30	12,877	49.6	13.9	2.4	7.9	26.2
	Oct	31	13,874	48.4	18.9	3.1	8.1	21.5
	Nov	30	13,994	39.6	23.8	2.5	4.9	29.2
	Dec	31	14,930	43.6	20.9	3.0	8.6	23.9
2005	Jan	31	14,748	56.1	12.9	1.7	3.1	26.2
	Feb	28	12,850	57.8	12.7	1.1	4.1	24.3
	Mar	31	13,590	43.6	16.8	3.0	10.8	25.8
	Apr	30	12,591	58.2	21.6	2.3	4.7	13.2
	May	31	12,385	63.6	21.3	2.0	4.4	8.7
	Jun	30	11,855	57.0	16.1	1.8	5.5	19.6
	Jul	31	12,409	70.3	17.1	1.5	2.8	8.3
	Aug	31	12,737	77.0	14.8	1.1	2.5	4.6
	Sep	30	12,462	56.2	12.0	3.8	4.0	24.0

<sup>9</sup> See <http://www.naoj.org/Observing/Telescope/ImageQuality/Seeing>.

TABLE 7 (Continued)

Year	Month	Number						
		of Nights	$N_{data}$	CLR	THN	MED	CDY	RNY
	Oct	31	13,579	52.0	15.3	4.5	10.4	17.8
	Nov	30	14,078	46.8	19.4	3.9	10.0	19.9
	Dec	31	14,866	79.5	12.9	0.7	3.1	3.8

NOTES.—CLR, THN, MED, CDY, and RNY mean the whole-sky cloud conditions CLEAR, THIN-or-PARTIAL, MEDIUM, CLOUDY, and RAINY, respectively, and are given in percentage values. No data other than analog vision were obtained between 2002 January and May.

<sup>a</sup> CLR, THN, and MED combined.

<sup>b</sup> CLR and THN combined.

### 6. CONCLUSIONS

We have developed an infrared cloud monitor weather system that has been very successfully supporting an unmanned robotic telescope. It sees almost the whole sky in thermal infrared, with no field deformation, it sensitively detects thin, high-altitude clouds, automatically evaluates sky conditions, and withstands outdoor environments for several months without maintenance. With this system, the MAGNUM observatory has been achieving unmanned automated observation at Haleakala for more than 4 years. Its evaluation of the whole-sky cloud condition as being photometric, observable, or nonob-

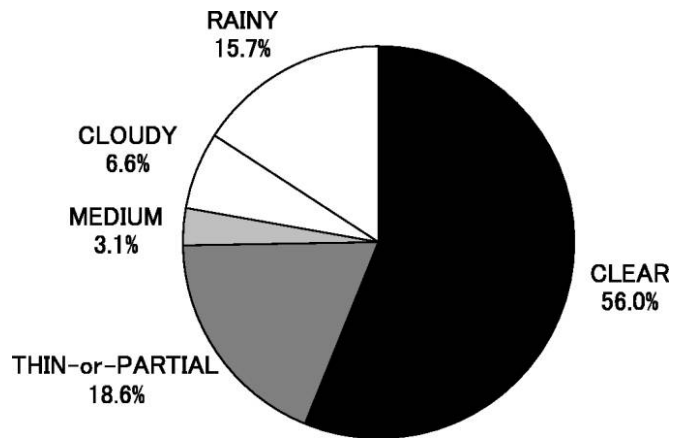


FIG. 14.—Distribution of whole-sky cloud conditions at night at Haleakala over 5 years between 2001 January and 2005 December. Percentages shown are weighed by the number of nights per month. The percentage for combined conditions between 2001 January and July is divided into respective conditions, according to their average proportions after 2001 August.

servable seems mainly to be successful. It also proves that for optical and near-infrared observations, the Haleakala site is comparable to Mauna Kea. Copies of our cloud monitor are now used for many similar systems at sites all around the world, including the Atacama region in the northern part of Chile.

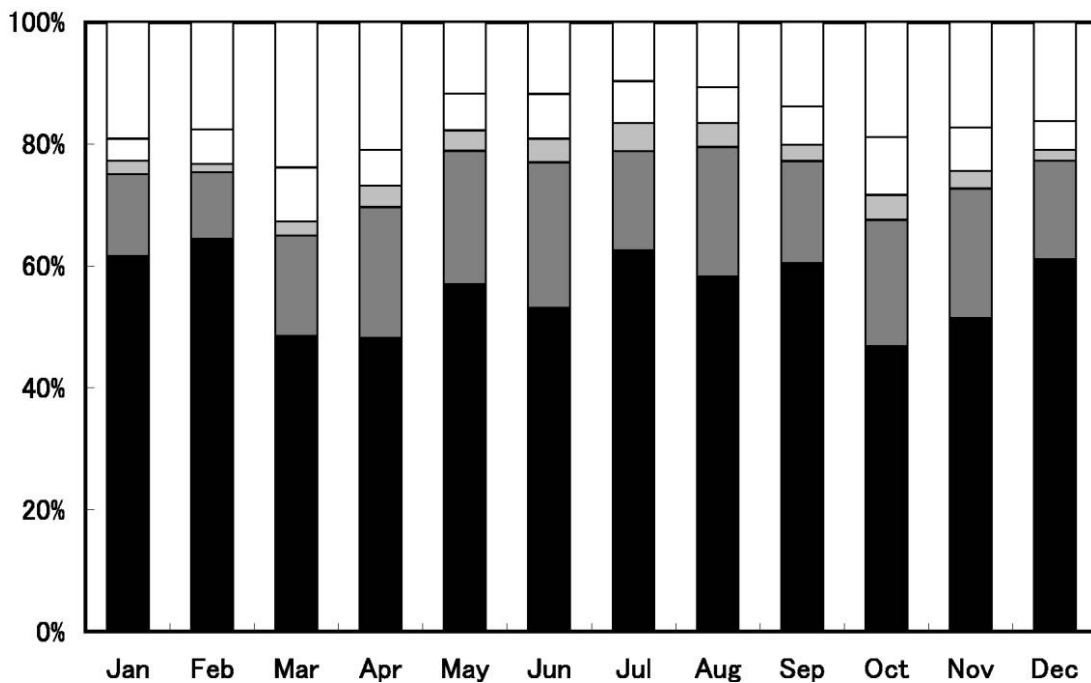


FIG. 15.—Mean monthly distribution of whole-sky cloud conditions at the Haleakala site over 5 years, from 2001 to 2005: CLEAR (black), THIN-or-PARTIAL (dark gray), MEDIUM (light gray), CLOUDY (bottom white), and RAINY (top white). The same corrections performed in Fig. 14 were done for the data between 2001 January and July.

The development of our cloud monitor was supported by the Advanced Technology Center at the National Astronomical Observatory of Japan. We are grateful to the Technical Center of Nagoya University for use of their ultraprecise turning machine. We thank H. Takami and N. Takato for helpful discussions and advice on development. We also thank M. Doi, K. Motohara, and colleagues at the Haleakala Observatories for their help

with facility maintenance. This research has been supported partly by the Grant-in-Aid of Scientific Research (10041110, 10304014, 11740120, 12640233, 14047206, 14253001, 14540223, 16740106, and 17104002) and COE Research (07CE2002) of the Ministry of Education, Science, Culture and Sports of Japan.

## REFERENCES

- Bradley, E. S., Roberts, L. C., Jr., Bradford, L. W., Skinner, M. A., Nahrstedt, D. A., Waterson, M. F., & Kuhn, J. R. 2006, *PASP*, 118, 172
- Chahl, J. S., & Srinivasan, M. V. 1997, *Appl. Opt.*, 36, 8275 (erratum 38, 1196 [1999])
- Committee on Extensions to the Standard Atmosphere. 1976 *US Standard Atmosphere 1976* (Washington: GPO)
- Cox, A. N., ed. 2000, *Allen's Astrophysical Quantities* (4th ed.; New York: AIP)
- Hogg, D. W., Finkbeiner, D. P., Schlegel, D. J., & Gunn, J. E. 2001, *AJ*, 122, 2129
- Hull, C., Limmongkol, S., & Siegmund, W. A. 1994, *Proc. SPIE*, 2199, 852
- Kobayashi, Y., Yoshii, Y., & Minezaki, T. 2004, *Astron. Nachr.*, 235, 537
- Kobayashi, Y., et al. 1998, *Proc. SPIE*, 3354, 769
- . 2003, *Proc. SPIE*, 4837, 954
- Mallama, A., & Degnan, J. J. 2002, *PASP*, 114, 913
- Platt, C. M. R., & Stephens, G. L. 1980, *J. Atmos. Sci.*, 37, 2314
- Shamir, H., & Nemiroff, R. J. 2005, *PASP*, 117, 972
- Takato, N., Okada, N., Kosugi, G., Suganuma, M., Miyashita, A., & Uruguchi, F. 2002, *Proc. SPIE*, 4837, 872
- Yoshii, Y. 2002, in *New Trends in Theoretical and Observational Cosmology*, ed. K. Sato & T. Shiromizu (Tokyo: Universal Academy Press), 235
- Yoshii, Y., Kobayashi, Y., & Minezaki, T. 2003, *BAAS*, 202, 38.03